

Fully gapped s -wave-like superconducting state and electronic structure in $\text{Ir}_{0.95}\text{Pd}_{0.05}\text{Te}_2$ single crystals with strong spin-orbital coupling

D. J. Yu,¹ F. Yang,¹ Lin Miao,¹ C. Q. Han,¹ Meng-Yu Yao,¹ Fengfeng Zhu,¹ Y. R. Song,¹ K. F. Zhang,¹ J. F. Ge,¹ X. Yao,¹ Z. Q. Zou,² Z. J. Li,³ B. F. Gao,³ Canhua Liu,¹ D. D. Guan,¹ C. L. Gao,^{1,*} Dong Qian,^{1,†} and Jin-feng Jia¹

¹Key Laboratory of Artificial Structures and Quantum Control (Ministry of Education), Department of Physics and Astronomy, Shanghai Jiao Tong University, Shanghai 200240, China

²Center for Analysis and Testing, Shanghai Jiao Tong University, Shanghai 200240, China

³State Key Laboratory of Functional Materials for Informatics, Shanghai Institute of Microsystem and Information Technology, Chinese Academy of Sciences, Shanghai 200050, China

(Received 31 December 2013; revised manuscript received 12 February 2014; published 4 March 2014)

Due to the large spin-orbital coupling in the layered $5d$ -transition metal chalcogenides compound, the occurrence of superconductivity in doped $\text{Ir}_{2-x}\text{Pd}_x\text{Te}_2$ offers a good chance to search for possible topological superconducting states in this system. We did comprehensive studies on the superconducting properties and electronic structures of single crystalline $\text{Ir}_{0.95}\text{Pd}_{0.05}\text{Te}_2$ samples. The superconducting gap size, critical fields, and coherence length along different directions were experimentally determined. Macroscopic bulk measurements and microscopic low temperature scanning tunneling spectroscopy results suggest that $\text{Ir}_{0.95}\text{Pd}_{0.05}\text{Te}_2$ possesses a BCS-like s -wave state. No sign of zero bias conductance peak was found in the vortex core at 0.4 K.

DOI: [10.1103/PhysRevB.89.100501](https://doi.org/10.1103/PhysRevB.89.100501)

PACS number(s): 74.70.Xa, 74.25.Ha

As a new quantum state of matter, topological insulators (TIs) were theoretically proposed involving band inversion due to strong spin-orbital coupling (SOC) and experimentally discovered in compounds with high- Z elements such as HgTe , Bi-based compounds, Sb_2Te_3 [1–7], and so on. Very soon after the discovery of TIs, extensive studies have been carried out in topological matters and topological phenomenon. One of the important topological states is so-called topological superconductors (TSCs) [2,8,9], in which the zero-energy mode of Majorana fermion that is proposed to be useful in topological quantum computation may harbor [10]. Previously, the most expected TSC is unconventional p -wave superconductor Sr_2RuO_4 [11,12]. After the conception of topological insulators, many effects for searching the possible TSCs have been put on the superconductors with large spin-orbital coupling. The possible candidates include Cu-intercalated topological insulator $\text{Cu}_x\text{Bi}_2\text{Se}_3$ [13,14], In-doped SnTe [15], and so on. Some signs of zero energy conductance peaks that may be related to Majorana fermion were observed [15–17]. Recently, superconductivity was realized in a layered chalcogenide with high- Z elements: IrTe_2 with Pd, Pt, and Cu [18–21] substitution or intercalations. Because of the large SOC in this material, it becomes a possible candidate of TSC [18]. Though IrTe_2 is a layered compound, it is different from typical layered transitional metal dichalcogenides; IrTe_2 layers are bonded to each other by significant Te-Te bonding rather than weak van der Waals force. IrTe_2 undergoes a structural phase transition from trigonal phase to triclinic phase at temperature of ~ 270 K [18,22]. The origin of structure transition is still under debate. Fermi surface (FS) nesting, the Rice-Scott saddle-point mechanism, orbital-induced Peierls instability, crystal field effects, the interlayer hybridization states, the local bonding instability, and the anionic depolymerization transition have been proposed [23]. With intercalation or substitution at the Ir

sites of some nonmagnetic elements, the structural transition can be suppressed and bulk superconductivity is induced with T_c up to ~ 3 K. It will be very interesting to know the details of the superconducting state and how the electronic structures evolve in this system. In this Rapid Communication, the superconducting properties and electronic structures in the $\text{Ir}_{0.95}\text{Pd}_{0.05}\text{Te}_2$ single crystals were studied by means of dc magnetic susceptibility, electrical resistance, band structure measurements, and scanning tunneling microscopy and spectroscopy (STM/STS) measurements. The superconducting gap size, coherence length, vortex states, and band structures were experimentally determined directly. We find that $\text{Ir}_{0.95}\text{Pd}_{0.05}\text{Te}_2$ has a fully gapped weak-coupling BCS s -wave-like superconducting state and nearly identical low energy band structure as parent compound IrTe_2 . No zero bias conductance peak was detected in the vortex core, so a topological superconducting state can be ruled out in this system at 0.4 K.

High quality single crystals of $\text{Ir}_{0.95}\text{Pd}_{0.05}\text{Te}_2$ were grown using the chemical vapor transport method with iodine as a carrier agent. Doped samples were grown in a single step process in which iridium (99.99%), tellurium (99.999%), palladium (99.95%), and iodine powders (99.99%) according to the stoichiometric ratio were sealed in an evacuated fused silica ampoule. They were grown with a temperature gradient of 60°C with the hot end held at 880°C . The sample size is about $1\text{ mm} \times 1\text{ mm} \times 0.2\text{ mm}$. As a comparison, parent compound IrTe_2 single crystals were grown out of Te flux using the same method as the previous works [19,24]. The crystal structure was checked by x-ray diffraction (XRD) (Bruker) with $\text{Cu } K_\alpha$ line. The angle-resolved photoemission spectroscopy (ARPES) measurements were performed using 40–120 eV photons at Advanced Light Source beamlines 4.0.3 using Scienta R4000 analyzers with base pressures better than 5×10^{-11} torr. Energy resolution is better than 15 meV and angular resolution is better than 0.02° . Low temperature STM/STS experiments were carried out in ultrahigh vacuum with a base pressure better than 1×10^{-10} Torr. Tungsten tips are used for STM/STS measurements. The dI/dV data of

*clgao@sjtu.edu.cn

†dqian@sjtu.edu.cn

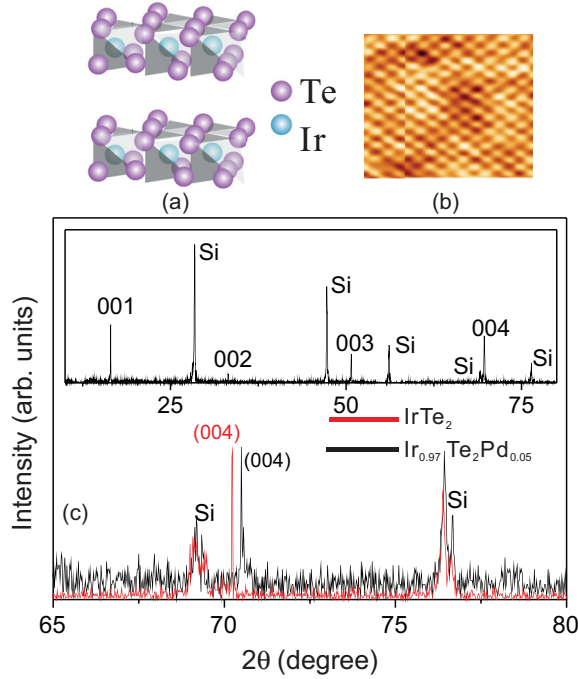


FIG. 1. (Color online) (a) Sketch of the IrTe_2 crystal structure. (b) Atomic resolved STM image on the cleaving surface of $\text{Ir}_{0.95}\text{Pd}_{0.05}\text{Te}_2$ ($V = 1.5$ V; $I = 190$ pA). (c) XRD spectra of the single crystal $\text{Ir}_{0.95}\text{Pd}_{0.05}\text{Te}_2$ and IrTe_2 at (004) peak. The inset is the large range XRD spectra.

superconducting gaps were obtained via lock-in technique with modulation signal voltage 0.05 mV with a frequency of 985 Hz. The samples are cleaved *in situ* at 30 K as well as at room temperature. The dc magnetization measurements were performed on a Quantum Design Physical Property Measurement System (PPMS). Temperature and magnetic fields dependent resistance measurements were carried out in the PPMS using the standard four-point probe technique with silver paste used for the contacts.

Figure 1 shows the crystal structure of IrTe_2 and the XRD spectra from the doped and the undoped crystals. Seen from Fig. 1(c), except for the Si reference peak, all the diffraction peaks can be indexed by (00l) peaks according to $P3m1$ structure from $\text{Ir}_{1-x}\text{Pd}_x\text{Te}_2$ with FWHM less than 0.05° , which indicates the high crystalline quality of the samples. Si reference peaks were used to correct the system error. The (004) peaks were used to calculate the c -axis lattice constant. Based on the Bragg condition, the calculated c -axis lattice constant is 5.386 Å and 5.372 Å for IrTe_2 and $\text{Ir}_{1.95}\text{Pd}_{0.05}\text{Te}_2$, respectively. After $x = 0.05$ Pd doping, the lattice contracts by $\sim 0.26\%$ which is consistent with the Pd-Te substitution known from the powder samples [18]. After cleaving, the surface is Te terminated. Figure 1(b) shows a well-ordered hexagonal lattice on the surface.

Typical low-temperature dc magnetic signal and electrical resistance of $\text{Ir}_{0.95}\text{Pd}_{0.05}\text{Te}_2$ samples are shown in Fig. 2. A diamagnetic behavior, characteristic of a superconducting state, is observed below ~ 2.5 K. The magnetization signal obtained at 2.1 K is about 60% of that expected for full diamagnetism. This represents a conservative lower limit

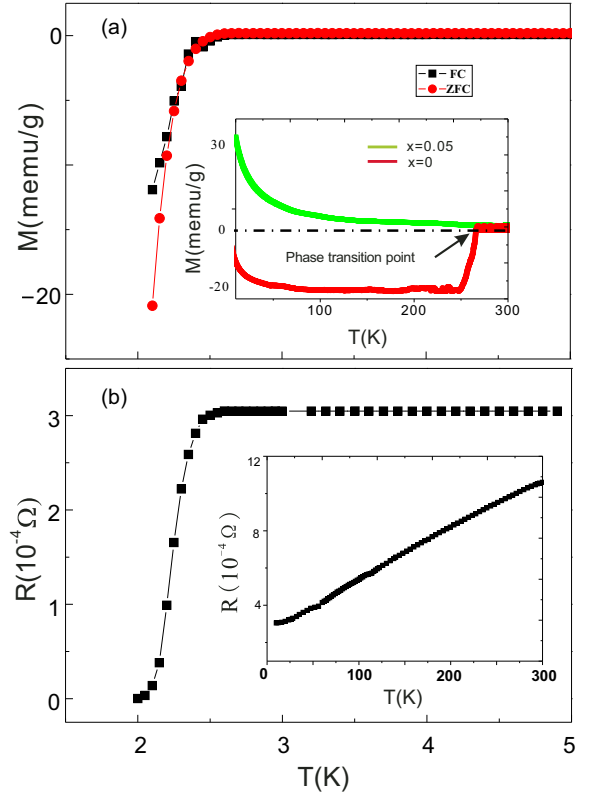


FIG. 2. (Color online) (a) Temperature dependence of the dc magnetization under 20 G field of $\text{Ir}_{0.95}\text{Pd}_{0.05}\text{Te}_2$ with zero field cooling (ZFC) and field cooling (FC). Diamagnetic signal is observed at ~ 2.5 K. Inset: temperature dependence of the dc magnetization of $\text{Ir}_{0.95}\text{Pd}_{0.05}\text{Te}_2$ and IrTe_2 with 2 T magnetic field applied perpendicular to the ab plane. (b) Temperature dependence of the resistance of $\text{Ir}_{0.95}\text{Pd}_{0.05}\text{Te}_2$ crystals with current flowing in the ab plane. Superconducting onset temperature is ~ 2.5 K. Inset: temperature dependence of the resistance for $\text{Ir}_{0.95}\text{Pd}_{0.05}\text{Te}_2$ with 2 T magnetic field applied perpendicular to the ab plane.

to the true superconducting volume fraction because the diamagnetic magnetization is still decreasing steeply at the temperature where the field is applied for the zero field cooling measurement. Figure 2(b) shows the temperature dependence of the resistance of $\text{Ir}_{0.95}\text{Pd}_{0.05}\text{Te}_2$, measured in the ab plane. Consistent with magnetic measurement, resistance of the sample decreases at ~ 2.5 K and reaches zero at ~ 2 K, suggesting bulk superconductivity. As presented in the inset of Fig. 2(a), with $x = 0.05$ Pd substitution the magnetic signal increases monotonically in the doped samples with the decrease of temperature under the magnetic field of 2 T. The structure phase transition is completely suppressed in $\text{Ir}_{0.95}\text{Pd}_{0.05}\text{Te}_2$, while IrTe_2 shows a sharp transition at ~ 270 K [18], marked by a black arrow.

Detailed measurements of the magnetic signals and the resistance as a function of magnetic fields are presented in Fig. 3. Figures 3(a) and 3(b) show the magnetization curves at different temperatures (from 2.1 K to 2.8 K) along out-of-plane (\perp) and in-plane (\parallel) direction, respectively. Seen from the magnetization curves, $\text{Ir}_{0.95}\text{Pd}_{0.05}\text{Te}_2$ has typical type-II superconductor behavior. As shown in Figs. 3(a) and 3(b), the blue arrows mark the position of $H_{c2\perp}$ and $H_{c2\parallel}$, where diamagnetic

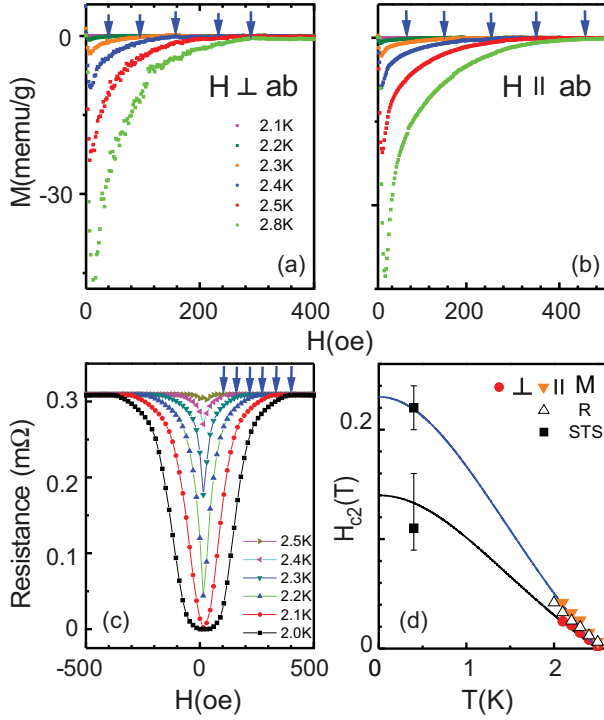


FIG. 3. (Color online) $M(H)$ curves at $T = 2.1$ K, 2.2 K, 2.3 K, 2.4 K, 2.5 K, and 2.8 K with magnetic field (a) perpendicular to the ab plane. (b) Parallel to the ab plane. (c) Resistance as a function of magnetic field applied in the ab plane at $T = 2.0$ K, 2.1 K, 2.2 K, 2.3 K, 2.4 K, and 2.5 K. Blue arrows marking the position of $H_{c2}(T)$. (d) $H_{c2}(T)$ determined from $M(H)$, $R(H)$, and STS data at different temperatures. Solid curves are fitting curves to the magnetic signal measurements.

signals disappear at different temperatures. In the resistance data [Fig. 3(c)], the upper critical field H_{c2} was defined at the superconducting onset temperature. Figure 3(d) summarizes the H_{c2} as a function of temperature. The linear temperature dependence close to T_c is obtained for H_{c2} , suggesting the dominance of only one type of bulk carrier, which is consistent with ARPES measurement shown below. The solid line is the fitting to Werthamer-Helfand-Hohenberg (WHH) theory based on the magnetic measurements. We obtained the upper critical field at zero temperature $H_{c2,\perp}(0) = 0.16 \pm 0.05$ T and $H_{c2,\parallel}(0) = 0.33 \pm 0.05$ T. From $H_{c2,\perp}$, the coherence length $\xi_{\parallel} = \sqrt{\Phi_0/2\pi H_{c2,\perp}} = 45$ nm is obtained, while from $H_{c2,\parallel}$ we use $\xi_{\perp} \xi_{\parallel} = \Phi_0/2\pi H_{c2,\parallel}$ and obtain $\xi_{\perp} = 22$ nm. So the dimensionless anisotropy parameter $\gamma = \xi_{\parallel}/\xi_{\perp} \sim 2$, which is smaller than another layered superconductor NbSe₂ ($\gamma \sim 3$).

The properties of the superconducting state are further explored by low temperature STM/STS. Figure 4(a) shows the typical STS spectra obtained on the cleaved surface at 0.4 K. Well-defined coherence peaks corresponding to the superconducting state were observed clearly. The STS spectra can be nicely fitted using BCS-type *s*-wave formula, which gives a superconducting gap of 0.36 ± 0.02 meV at 0.4 K. Assuming the gap follows BCS theory, $\Delta(T) = \Delta(0)(1 - T/T_c)^{1/2}$, we get $\Delta(0) \sim 0.39 \pm 0.02$ meV, yielding the BCS ratio $2\Delta/k_B T_c \sim 3.6$. This value indicates a weak-coupling BCS-type superconductor (for weak-coupling limit *s*-wave,

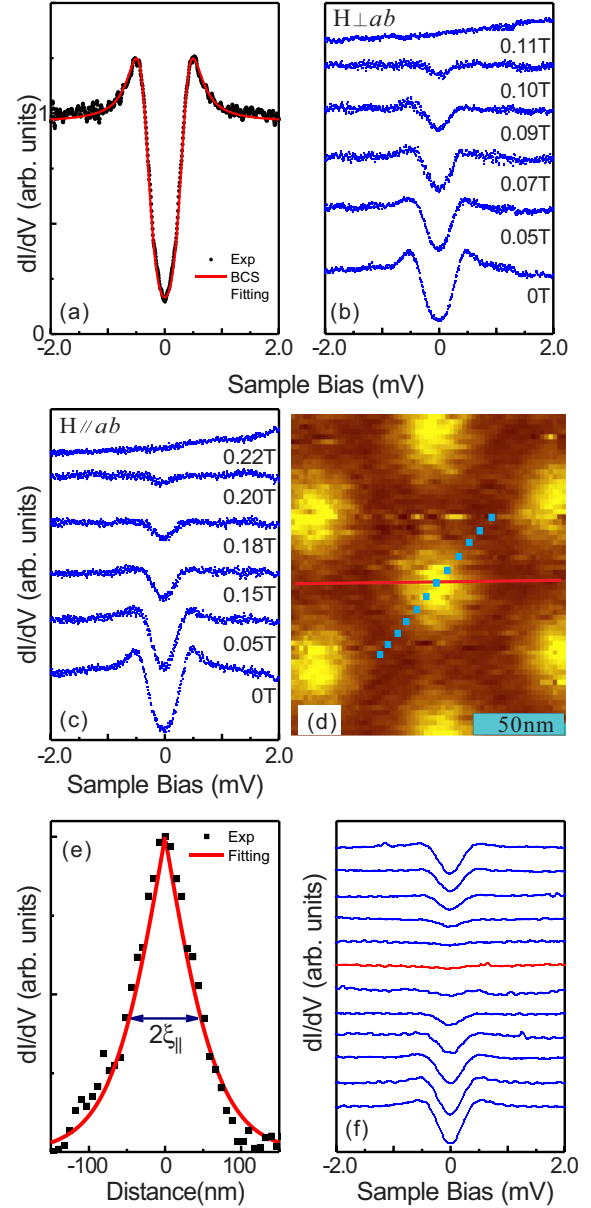


FIG. 4. (Color online) (a) Typical superconducting gap (dI/dV spectra) measured at 0.4 K. The distance between the tip and sample is set to be ~ 1 nm. Superconducting gap is further confirmed by checking the evolution of the dI/dV spectra with magnetic fields (b) perpendicular to the ab and (c) parallel to the ab plane. (d) Superconducting vortex lattice measured by STS mapping. Applied magnetic field is 0.05 T. Red curve shows how to get the vortex's line profile. (e) Line profile of the single vortex. Red curve is the fitting curve to extract the coherence length. (f) dI/dV curves measured at different position according to blue dots in (d).

BCS ratio ~ 3.5). The STS spectra as a function of applied magnetic fields are shown in Figs. 4(b) and 4(c). With the increase of applied magnetic field, the coherence peak faded away gradually. The energy gap disappears at about 0.11 T and 0.22 T when the magnetic field is perpendicular or parallel to the ab plane. It is worth noting that these two values are position dependent due to the existence of the vortex [vortices are shown in Fig. 4(d)] and the variation is much

smaller when the magnetic field is applied in the ab plane. Nevertheless, the upper critical fields obtained in STS are well consistent with macroscopic bulk measurements as shown in Fig. 3(d). Superconducting vortex was observed by STS mapping. Figure 4(d) shows the vortex with nice close-packed arrangement. From the size of the vortex, as shown in Fig. 4(e), the in plane coherence length $\xi(T = 0.4 \text{ K})$ of $\sim 51 \pm 5 \text{ nm}$ is obtained from the fitting of the line profile [red line in Fig. 4(d)] of the vortex, which is nearly consistent with the value from the bulk magnetic measurement. Small BCS ratio, s -wave-like gap function and long coherence length suggest that $\text{Ir}_{0.95}\text{Pd}_{0.05}\text{Te}_2$ is a fully gapped and weak coupling BCS-type s -wave superconductor. In addition, we carefully checked the STS at different positions of vortex as shown in Fig. 4(f). The red curve in Fig. 4(f) is collected right at the center of a vortex. Outside the vortex, there is a superconducting gap and the gap closes at the center of the vortex. Under our experimental temperature (0.4 K), no sign of zero bias conductance peak was observed at any position of vortex, which means even if there will be nontrivial superconducting states, much lower temperature is needed. From the STS measurement, we think we can rule out the possibility of a topological superconducting state in this system at 0.4 K.

Finally, the electronic structures of $\text{Ir}_{0.95}\text{Pd}_{0.05}\text{Te}_2$ are studied by ARPES. Same as IrTe_2 , the energy bands of $\text{Ir}_{0.95}\text{Pd}_{0.05}\text{Te}_2$ show strong k_z dispersion. By tuning incident photon energy, we can change the detectable momentum along the normal direction (k_z). In-plane FS at different k_z was obtained by integrating the spectra weight with an energy window of 15 meV at Fermi energy. Changing of FS topology was observed in previous studies in IrTe_2 below and above the phase transition temperature [23,25]. Figure 5(a) shows the FS of $\text{Ir}_{0.95}\text{Pd}_{0.05}\text{Te}_2$ measured at 30 K overlaid with the room temperature FS (green and blue dotted lines) of IrTe_2 from Ref. [23] at the exact same k_z ($\sim 0.8\pi$) point using 90 eV photon energy. Clearly, after Pd substitution, the FS of superconducting samples at low temperature is the same as that of IrTe_2 at room temperature. There is one outer big FS, three small Fermi pockets, and a tiny Fermi pocket around zone center. Meanwhile, the three small Fermi pockets [blue dotted lines in Fig. 5(a)] disappear at 30 K in IrTe_2 samples [23]. Figures 5(c) and 5(d) show energy bands along the direction indicated by the yellow dotted line in Fig. 5(a). Known from the band mapping, all the FSs are formed by holelike bands. Since $\text{Ir}_{0.95}\text{Pd}_{0.05}\text{Te}_2$ has no phase transition but has identical FS as that of the IrTe_2 sample above phase transition temperature, it implies that itinerant origins such as FS nesting or saddle point nesting may not play key roles for the phase transition in this system. Phase transition is more likely related to local phenomena. For example, the depolymerization-polymerization of Te bonds was proposed to be involved in the phase transition [26]. And it was also proposed that Ir $5d$ orbital reconstruction governed the charge and orbital instability in IrTe_2 [19]. In addition, charge modulation originated from the periodic dimerization of Te atoms was observed in previous STM experiments [27]. Figure 5(b) presents the FS near π point. At this k_z point, the saddle point (marked as “S” in the figure) observed in IrTe_2 [23] remains in $\text{Ir}_{0.95}\text{Pd}_{0.05}\text{Te}_2$, which leaves the possibility that the superconducting instability can be related to the van

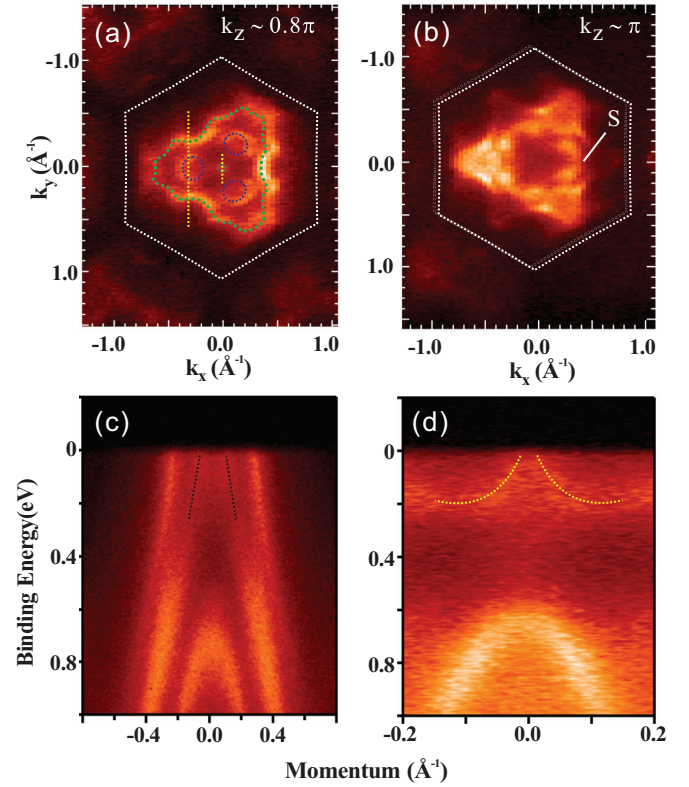


FIG. 5. (Color online) (a) Fermi surface at $k_z \sim 0.8\pi$ on $\text{Ir}_{0.95}\text{Pd}_{0.05}\text{Te}_2$ measured at 30 K. Green and blue dotted curves present the measured Fermi surface at room temperature on IrTe_2 . No obvious difference was observed between $\text{Ir}_{0.95}\text{Pd}_{0.05}\text{Te}_2$ and IrTe_2 . (b) FS of $\text{Ir}_{0.95}\text{Pd}_{0.05}\text{Te}_2$ at $k_z \sim \pi$. “S” labels the same saddle point as in IrTe_2 [23]. (c),(d) ARPES spectra at the momentum space as indicated in (a) by yellow dotted line. Black dotted line marks the holelike bands crossing the Fermi level that sink beneath the Fermi level in IrTe_2 at low temperature.

Hove singularity at saddle points [23]. This scenario could be studied by ultralow temperature ARPES experiments in the future.

In summary, we did comprehensive studies of the superconducting properties and electronic structures of $\text{Ir}_{0.95}\text{Pd}_{0.05}\text{Te}_2$. By combination of the macroscopic and microscopic measurements, the superconducting gap size, coherence length, and electronics structures as well as the vortex states were determined. At 0.4 K, the samples present a BCS-type s -wave-like superconducting behavior. Though no exotic superconducting state was found in this system, the hexagonal lattice structure of $\text{Ir}_{0.95}\text{Pd}_{0.05}\text{Te}_2$ is very suitable for epitaxial growth of TIs. In our previous work, Bi_2Se_3 (Bi_2Te_3) TI films were successfully grown on s -wave superconductor NbSe_2 [28,29]. This type of heterostructure utilizing the superconducting proximity effect perpendicular to the ab plane is called vertical geometry. Superconducting $\text{Ir}_{1-x}\text{Pd}_x\text{Te}_2$ will be another excellent candidate for this geometry since its vertical coherence length is much larger than that of NbSe_2 ($\xi \sim 3 \text{ nm}$). The heterostructure of TI/ $\text{Ir}_{1-x}\text{Pd}_x\text{Te}$ can be a good candidate for exploring topological superconductor related phenomena in the future.

This work is supported by National Basic Research Program of China (Grants No. 2012CB927401, No. 2011CB921902, No. 2013CB921902, and No. 2011CB922200), NSFC (Grants No. 91021002, No. 10904090, No. 11174199, No. 11227404, and No. 11134008), Strategic Priority Research Program of the Chinese Academy of Science (Grant No. XDB04010600) and the SCST, China (Grants No. 12JC1405300, No. 13QH1401500, No.

10JC1407100, No. 10PJ1405700, and No. 11PJ405200). The Advanced Light Source is supported by the Director, Office of Science, Office of Basic Energy Sciences, of the US Department of Energy under Contract No. DE-AC02-05CH11231. D.Q. acknowledges additional supports from the Top-notch Young Talents Program and the Program for Professor of Special Appointment (Eastern Scholar) at Shanghai Institutions of Higher Learning.

-
- [1] M. Z. Hasan and C. L. Kane, *Rev. Mod. Phys.* **82**, 3045 (2010).
 - [2] X.-L. Qi and S.-C. Zhang, *Rev. Mod. Phys.* **83**, 1057 (2011).
 - [3] B. A. Bernevig, T. L. Hughes, and S. C. Zhang, *Science* **314**, 1757 (2006).
 - [4] D. Hsieh, D. Qian, L. Wray, Y. Xia, Y. S. Hor, R. J. Cava, and M. Z. Hasan, *Nature (London)* **452**, 970 (2008).
 - [5] Y. Xia, D. Qian, D. Hsieh, L. Wray, A. Pal, H. Lin, A. Bansil, D. Grauer, Y. S. Hor, R. J. Cava, and M. Z. Hasan, *Nature Phys.* **5**, 398 (2009).
 - [6] Y. L. Chen, J.-H. Chu, J. G. Analytis, Z. K. Liu, K. Igarashi, H.-H. Kuo, X. L. Qi, S. K. Mo, R. G. Moore, D. H. Lu, M. Hashimoto, T. Sasagawa, S. C. Zhang, I. R. Fisher, Z. Hussain, and Z. X. Shen, *Science* **325**, 178 (2009).
 - [7] H. J. Zhang, C. X. Liu, X. L. Qi, X. Dai, Z. Fang, and S. C. Zhang, *Nat. Phys.* **5**, 438 (2009).
 - [8] A. P. Schnyder, S. Ryu, A. Furusaki, and A. W. W. Ludwig, *Phys. Rev. B* **78**, 195125 (2008).
 - [9] X. L. Qi, T. L. Hughes, S. Raghu, and S. C. Zhang, *Phys. Rev. Lett.* **102**, 187001 (2009).
 - [10] L. Fu and C. L. Kane, *Phys. Rev. Lett.* **100**, 096407 (2008).
 - [11] A. P. Mackenzie and Y. Maeno, *Rev. Mod. Phys.* **75**, 657 (2003).
 - [12] Y. Maeno, S. Kittaka, T. Nomura, S. Yonezawa, and K. Ishida, *J. Phys. Soc. Jpn.* **81**, 011009 (2012).
 - [13] L. Fu and E. Berg, *Phys. Rev. Lett.* **105**, 097001 (2010).
 - [14] L. A. Wray, S. Xu, Y. Xia, D. Qian, A. V. Fedorov, H. Lin, A. Bansil, L. Fu, Y. S. Hor, R. J. Cava, and M. Z. Hasan, *Phys. Rev. B* **83**, 224516 (2011).
 - [15] S. Sasaki, Z. Ren, A. A. Taskin, K. Segawa, L. Fu, and Y. Ando, *Phys. Rev. Lett.* **109**, 217004 (2012).
 - [16] S. Sasaki, M. Kriener, K. Segawa, K. Yada, Y. Tanaka, M. Sato, and Y. Ando, *Phys. Rev. Lett.* **107**, 217001 (2011).
 - [17] V. Mourik, K. Zuo, S. M. Frolov, S. R. Plissard, E. P. A. M. Bakkers, and L. P. Kouwenhoven, *Science* **336**, 6084 (2012).
 - [18] J. J. Yang, Y. J. Choi, Y. S. Oh, A. Hogan, Y. Horibe, K. Kim, B. I. Min, and S. W. Cheong, *Phys. Rev. Lett.* **108**, 116402 (2012).
 - [19] D. Ootsuki, Y. Wakisaka, S. Pyon, K. Kudo, M. Nohara, M. Arita, H. Anzai, H. Namatame, M. Taniguchi, N. L. Saini, and T. Mizokawa, *Phys. Rev. B* **86**, 014519 (2012).
 - [20] M. Kamitani, M. S. Bahramy, R. Arita, S. Seki, T. Arima, Y. Tokura, and S. Ishiwata, *Phys. Rev. B* **87**, 180501(R) (2013).
 - [21] S. Y. Zhou, X. L. Li, B. Y. Pan, X. Qiu, J. Pan, X. C. Hong, Z. Zhang, A. F. Fang, N. L. Wang, and S. Y. Li, *Europhys. Lett.* **104**, 27010 (2013).
 - [22] H. B. Cao, B. C. Chakoumakos, X. Chen, J. Q. Yan, M. A. McGuire, H. Yang, R. Custelcean, H. D. Zhou, D. J. Singh, and D. Mandrus, *Phys. Rev. B* **88**, 115122 (2013).
 - [23] T. Qian, H. Miao, Z. J. Wang, X. Liu, X. Shi, Y. B. Huang, P. Zhang, N. Xu, P. Richard, M. Shi, M. H. Upton, J. P. Hill, G. Xu, X. Dai, Z. Fang, H. C. Lei, C. Petrovic, A. F. Fang, N. L. Wang, and H. Ding, *arXiv:1311.4946*.
 - [24] A. F. Fang, G. Xu, T. Dong, P. Zheng, and N. L. Wang, *Sci. Rep.* **3**, 1153 (2013).
 - [25] D. Ootsuki, S. Pyon, K. Kudo, M. Nohara, M. Horio, T. Yoshida, A. Fujimori, M. Arita, H. Anzai, H. Namatame, M. Taniguchi, N. L. Saini, and T. Mizokawa, *J. Phys. Soc. Jpn.* **82**, 093704 (2013).
 - [26] Y. S. Oh, J. J. Yang, Y. Horibe, and S. W. Cheong, *Phys. Rev. Lett.* **110**, 127209 (2013).
 - [27] P. J. Hsu, T. Maurer, M. Vogt, J. J. Yang, Y. S. Oh, S. W. Cheong, M. Bode, and W. D. Wu, *Phys. Rev. Lett.* **111**, 266401 (2013).
 - [28] M. X. Wang, C. H. Liu, J. P. Xu, F. Yang, L. Miao, M. Y. Yao, C. L. Gao, C. Shen, X. C. Ma, X. Chen, Z. A. Xu, Y. Liu, S. C. Zhang, D. Qian, J. F. Jia, and Q. K. Xue, *Science* **336**, 52 (2012).
 - [29] J. P. Xu, C. H. Liu, M. X. Wang, J. F. Ge, Z. L. Liu, X. J. Yang, Y. Chen, Y. Liu, Z. A. Xu, C. L. Gao, D. Qian, F. C. Zhang, Q. K. Xue, and J.-F. Jia, *arXiv:1312.3713*.